THE JOURNAL OF PHYSICAL CHEMISTRY B

Article

pubs.acs.org/JPCB

Phase Transition and Dynamics in Imidazolium-Based Ionic Liquid Crystals through a Metastable Highly Ordered Smectic Phase

Yoko Nozaki,[†] Keito Yamaguchi,[†] Kenji Tomida,[†] Natsumi Taniguchi,[†] Hironori Hara,[†] Yoshinori Takikawa,[†] Koichiro Sadakane,[†] Kenji Nakamura,[†] Takashi Konishi,[‡] and Koji Fukao*[,†]

[†]Department of Physics, Ritsumeikan University, Noji-Higashi 1-1-1, Kusatsu 525-8577, Japan

[‡]Graduate School of Human and Environmental Studies, Kyoto University, Kyoto 606-8501, Japan

ABSTRACT: The phase transition behavior and dynamics of ionic liquid crystals, 1-methyl-3-alkylimidazolium tetrafluoroborate with various alkyl chain lengths, were investigated by X-ray scattering, differential scanning calorimetry, optical microscopy, and dielectric relaxation spectroscopy to elucidate the mechanism of their structural and phase changes. A metastable phase was found to appear via a supercooled smectic phase on cooling. In the metastable phase, disorder in the smectic phase is partially frozen; thus, the phase has order higher than that of the smectic phase but lower than that of the crystalline phase. During the subsequent heating process, the frozen disorder activates, and a crystalline phase appears in the supercooled smectic phase before entering the smectic phase. The relationship between the phase behavior and the dynamics of charge carriers such as ions is also discussed.

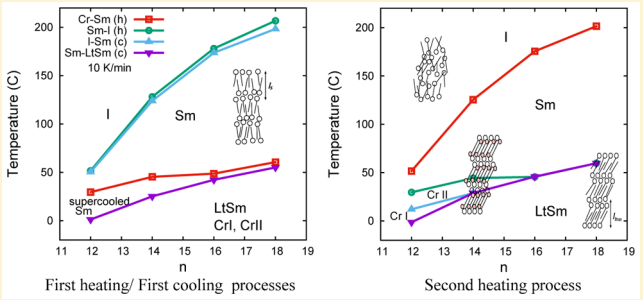

INTRODUCTION

An ionic compound with a melting temperature lower than 100 °C is generally defined as an ionic liquid (IL).[1−3] Many ILs have melting temperatures even lower than room temperature, although strong and long-range electrostatic interactions exist within the systems. Their chemical structure consists of cations such as alkylimidazolium and anions such as halogens and various ionic groups.[4−6] ILs may be regarded as novel environment-friendly solvents and useful electrochemical materials. Moreover, their chemical performance may be readily modified by varying their combination of cations and anions.

Ionic liquid crystals (ILCs) are ILs containing liquid crystalline molecules with a characteristic orientational capability, for example, long alkyl chains. Hence, ILCs can have high electric conductivity and characteristic mesoscopic structures formed via self-organization mechanism. Abundant experimental data have established that salts of 1-methyl-3-alkylimidazolium and the anions, $[C_n\text{mim}]X$, which have various alkyl chain lengths (X is BF_4, PF_6, etc.), exhibit several characteristic phase behaviors.[7−17] In many cases, the low-melting $[C_n\text{mim}]X$ shows an isotropic liquid phase at high temperatures and a crystalline phase at low temperatures. A mesophase, which has been found to be a smectic A phase in some cases, has been observed between the isotropic liquid and crystalline phases.[7,8] Several modifications of the crystalline phase have been observed, such as the bilayer, extended bilayer, and double bilayer. Solid−solid phase transitions of the crystalline state between structural modifications have also been observed.[14] In addition to the Sm phase, a smectic-like phase, which is often called a higher-order smectic phase, has been observed for 1-methyl-3-alkylimidazolium tetrafluoroborate ($[C_n\text{mim}]BF_4$).[10] Supercooling phenomena have been observed during the cooling process across phase transition temperatures for these salts.[8]

The higher-order smectic structure of imidazolium-based ILCs is often observed at low temperatures. Nevertheless, its stability and relationship to other phases and the dynamical behavior of ILCs have not yet been extensively investigated. In the present study, the phase transition behavior of $[C_n\text{mim}]BF_4$ with various alkyl chain lengths (n = 12, 14, 16, and 18) has been investigated by X-ray scattering, differential scanning calorimetry (DSC), optical microscopy (OM), and dielectric relaxation spectroscopy (DRS) to elucidate the mechanism of the structural and phase changes of imidazolium-based ILCs. The relationship between the phase change and the dynamics of charge carriers has also been elucidated through this study.

EXPERIMENTS

Sample Preparation. 1-Methylimidazolium, 1-bromododecane, 1-bromotetradecane, 1-bromohexadecane, 1-bromooctadecane, and sodium tetrafluoroborate were purchased from Tokyo Kasei (Tokyo). All of the reagents were used without further purification. For the synthesis of 1-methyl-3-dodecylimidazolium tetrafluoroborate $[C_{12}\text{mim}]BF_4$, 1-methyl-3-dodecylimidazolium bromide was first prepared by refluxing a mixture of 1-methylimidazole and excess bromododecane in an ethanol solution at 90 °C for several days. The resultant solution was dried under vacuum at 70 °C to evaporate the

Received: April 14, 2016
Revised: May 17, 2016
Published: May 19, 2016

DOI: 10.1021/acs.jpcb.6b03804
J. Phys. Chem. B 2016, 120, 5291−5300

ethanol and then dissolved in water. After the unreacted bromododecane was separated from the aqueous solution, an aqueous solution with a slight excess of sodium tetrafluoroborate was added to the solution and stirred for several days at room temperature. The resultant IL phase of 1-methyl-3-dodecylimidazolium tetrafluoroborate was separated from the aqueous phase and washed with water until the eluent remained clear following the addition of an aqueous $AgNO_3$ solution. The elimination of the Br ions from the ionic phase was confirmed by the Beilstein test. After complete evaporation of the remaining water, $[C_{12}mim]BF_4$ was dried under vacuum at 100 °C. Other $[C_nmim]BF_4$ samples (n = 14, 16, 18) were synthesized in a similar manner. The purity of $[C_nmim]BF_4$ was verified by ^1H NMR and elemental analysis. Found (%): C, 56.64; H, 9.40; N, 8.15; calcd for $C_{16}H_{31}BF_4N_2$ (%): C, 56.82; H, 9.24; N, 8.28 for $[C_{12}mim]BF_4$. Found (%): C, 59.27; H, 9.89; N, 7.52; calcd for $C_{18}H_{35}BF_4N_2$ (%): C, 59.02; H, 9.63; N, 7.65 for $[C_{14}mim]BF_4$. Found (%): C, 60.66; H, 10.18; N, 7.08; calcd for $C_{20}H_{39}BF_4N_2$ (%): C, 60.92; H, 9.97; N, 7.10 for $[C_{16}mim]BF_4$. Found (%): C, 62.31; H, 10.13; N, 6.59; calcd for $C_{22}H_{43}BF_4N_2$ (%): C, 62.56; H, 10.26; N, 6.63 for $[C_{18}mim]BF_4$.

DSC and OM. For the DSC measurements, a commercial instrument, Q200 (TA Instruments), was used. A powder sample of about 3 mg was placed in an aluminum pan with a lid. For OM, an optical microscope (Nikon Eclipse) was used under the crossed Nicol condition to observe the existence of optical anisotropy. Samples covered with glass substrates were mounted onto a hotstage (Linkam) for temperature control.

X-ray Scattering. Simultaneous measurements of two different geometries via small-angle X-ray scattering (SAXS) and wide-angle X-ray scattering (WAXS) measurements were performed at BL40B2 of SPring-8 to investigate the structure of $[C_nmim]BF_4$ over wide length scales. The X-ray wavelength λ was 0.8 Å, and the camera lengths were 1260 and 99.6 mm for SAXS and WAXS, respectively. The available q ranges for the SAXS and WAXS measurements were 0.3 $nm^{-1} < q < 3.5$ nm^{-1} and 4 $nm^{-1} < q < 40$ nm^{-1}, respectively, where q is the absolute value of the scattering vector and is defined as $q = (4\pi \sin\theta)/\lambda$, and 2θ is the scattering angle. A CCD camera with an image intensifier and an X-ray flat panel sensor were used as detector system for SAXS and WAXS, respectively. Samples were sealed into a metal ring covered with Kapton film with 7.5 μm thickness, which was then placed onto the hot stage of the microscope mounted on the sample holder on the beamline. Because of the strong X-ray source from synchrotron radiation (SR), the accumulation times required for one measurement for SAXS and WAXS were 100−500 ms and 2 s, respectively. Simultaneous SAXS and WAXS measurements were carried out with ramping at 10 K/min, so that the X-ray scattering results could be directly compared with those of the DSC measurements. The collected scattering intensity data were corrected to remove the contribution of background scattering and then converted into one-dimensional data by circular averaging.

DRS. An LCR meter (Agilent Technology, E4980A) was used for dielectric measurements over a frequency range of 20 Hz and 2 MHz. The $[C_nmim]BF_4$ sample was inserted into the 10 μm gap between indium tin oxide (ITO) glass and then used for the dielectric measurements. The electrode of the ITO glass was coated with polyimide films on which rubbing treatment was performed after coating. The area of the electrodes was 16 mm^2. The applied voltage was fixed at 100 mV. The observed complex impedance was converted into the complex electric capacitance C^*_{mes}. The complex dielectric permittivity ε^* was obtained by correcting the contribution of the electrical resistance R of the electrode of the ITO glass through the relation

$$\varepsilon^*(\omega)C_0 = \frac{C^*_{mes} + i\omega R|C^*_{mes}|^2}{1 - 2\omega R\ \mathrm{Im}(C^*_{mes}) + \omega^2R^2|C^*_{mes}|^2} \quad (1)$$

where $C_0 = \varepsilon_0(S/d)$, and $\omega = 2\pi f$. f is the frequency of the applied electric field (voltage), ε_0 is the dielectric permittivity of the vacuum, C_0 is a geometrical capacitance, S is the area of the electrode, and d is the thickness of the film or the distance between two electrodes. The complex dielectric permittivity ε^* is described by $\varepsilon^* = \varepsilon' - i\varepsilon''$, where ε' and ε'' are the real and imaginary components of ε^*.

RESULTS AND DISCUSSION

Phase Behavior Measured by DSC. Figure 1 shows the temperature dependence of the total heat flow observed during the first heating, first cooling, and second heating processes for $[C_nmim]BF_4$ (n = 12, 14, 16, 18). The heating and cooling rates were controlled at 10 K/min. For the first heating process, the as-prepared samples before measurement can be assumed to be in a crystalline phase (Cr I or Cr II, as explained later). As the temperature increases from 0 °C, the total heat flow begins to decrease at 20 °C, and large and small endothermic peaks for $[C_{12}mim]BF_4$ then appear at 29.5 and 51.6 °C, respectively. The two endothermic peak temperatures correspond to the temperatures for the transition between the crystalline phase and the smectic phase, and between the smectic phase and the isotropic liquid phase, as shown in previous studies.[8,10,11,16] In this paper, the isotropic liquid phase and the smectic A phase are denoted by I and Sm, respectively. The Cr I (or Cr II) to Sm and the Sm to I phase transition temperatures increase as n increases from 12 to 18. For example, the two phase transition temperatures are 48.7 and 178.0 °C for $[C_{16}mim]BF_4$ and 60.5 and 206.6 °C for $[C_{18}mim]BF_4$. These transition temperatures agree very well with the values reported in the literature.[8,10]

During the first cooling process, the transition from the I phase to the Sm phase can be observed. This is followed by the transition from the Sm phase to another solid phase at a temperature lower than the Cr I (or Cr II) to Sm transition temperature observed in the first heating process. The Sm phase changes to another solid phase through the supercooled smectic state during the cooling process.

In the second heating process, the thermal behaviors differ at different alkyl chain lengths. At n = 16 and 18, the temperature dependence of the total heat flow is almost identical to that observed in the first heating process. However, an exothermic peak appears at n = 14 after a large endothermic peak at 28.7 °C, and another endothermic peak then appears before the Sm phase. At n = 12, the thermal behavior is more complex; an exothermic peak, a small endothermic peak, and a large endothermic peak appear before the Sm phase. These changes are discussed in detail together with the X-ray results in the next section.

X-ray Scattering. As shown in Figure 1, the phase behavior of $[C_nmim]BF_4$ strongly depends on n of the alkyl part of $[C_nmim]BF_4$, especially at n = 12 and 14. In this section, the scattering patterns observed for the SAXS and WAXS regions by synchrotron radiation are used to elucidate the structural change accompanying with the thermal change during ramping at 10 K/min.

DOI: 10.1021/acs.jpcb.6b03804
J. Phys. Chem. B 2016, 120, 5291−5300

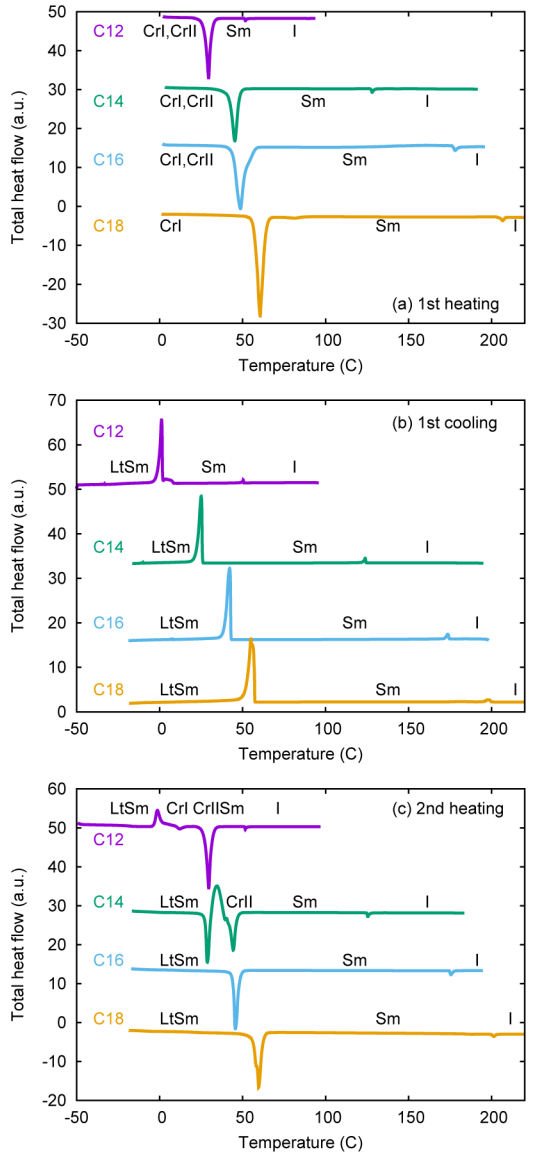

Figure 1. Temperature dependence of the total heat flow observed during the (a) first heating, (b) first cooling, and (c) second heating processes for $[C_n\text{mim}]BF_4$ (n = 12, 14, 16, 18). The ramping rate was 10 K/min. The direction from negative to positive value of the total heat flow corresponds to an exothermic process.

Previous studies have reported the crystalline modifications of this systems. In a crystalline modification, the alkyl chains are interdigitated in a regular manner both along the chain axis and perpendicular to the chain axis, forming a bilayer (Figure 2). In this paper, this crystalline structure is referred to as Cr I. The long period of the Cr I phase, l_{CrI}, is an increasing function of n. The value of l_{CrI} increases from 2.72 to 3.46 nm as n increases from 14 to 18 in the case of $[C_n\text{mim}]BF_4$.[11]

Other crystalline modifications include a double bilayer and an extended bilayer structure.[11] In the double bilayer, different conformations of the head groups are in alternating bilayers, as shown in Figure 2; in the extended bilayer, a lamellar structure of bilayers without alkyl chain interdigitation, that is, end-to-end packing of the alkyl chains, exists (the extended bilayer is not shown in Figure 2). In both bilayers, the long period along the chain axis is almost twice as large as that of the simple bilayer structure. This crystalline phase is termed Cr II in this

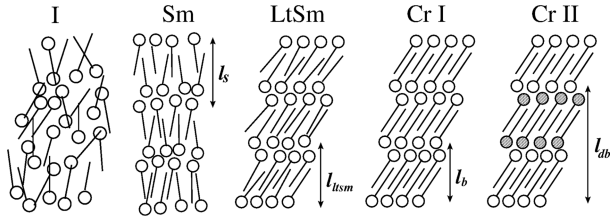

Figure 2. Schematic representations of the observed structural modifications in $[C_n\text{mim}]BF_4$. I: isotropic liquid phase; Sm: smectic A phase; LtSm: low-temperature smectic phase; Cr I: type I crystalline modification; Cr II: type II crystalline modification. A double bilayer structure for Cr II is shown here; however, an extended bilayer structure is also possible.

paper. Structural properties of the observed modifications in $[C_n\text{mim}]BF_4$ are listed in Table 1.

Table 1. Properties of the Observed Structural Modification in $[C_n\text{mim}]BF_4$[a]

name	I	Sm	LtSm	Cr I	Cr II
structure	random	lamella	bilayer	bilayer	double bilayer
longitudinal order	no	yes	yes	yes	yes
lateral order	no	no	yes or no	yes	yes

[a]I: isotropic liquid phase; Sm: smectic A phase; LtSm: low-temperature smectic phase; Cr I: type I crystalline modification; Cr II: type II crystalline modification. The relationship between the long periods of the various structural modifications is described by the relation $l_{Sm} > l_{LtSm} > l_{CrI}$, $l_{CrII} = 2l_{CrI}$, where l_{Sm}, l_{LtSm}, l_{CrI}, and l_{CrII} are the long periods of the Sm, LtSm, Cr I, and Cr II phases, respectively.

Phase Behavior of $[C_{12}\text{mim}]BF_4$. Figure 3 shows the changes with temperature of the observed X-ray scattering pattern for the first heating, first cooling, and second heating processes for $[C_{12}\text{mim}]BF_4$. The top of the figure corresponds to the temperature dependence of the peak positions observed for both the SAXS and WAXS regions, while the bottom of the figure corresponds to that of the peak intensities observed only for the SAXS regions.

First Heating Process. In the X-ray scattering patterns for the first heating process, many Bragg reflections are observed below 20 °C, as shown in Figure 3a. In the SAXS region, there are two strong peaks at 2.33 and 2.46 nm^{-1}, which correspond to 2.70 and 2.55 nm in real space, respectively. The existence of these spatial periodicities suggests that $[C_{12}\text{mim}]BF_4$ molecules are packed into an interdigitated structure, which corresponds to the Cr I phase, mentioned earlier. In addition, there was a mixture of two types of crystals with interdigitated structures that vary according to the chain conformations or to the degree of disorder.

As the temperature increases to 20 °C, the Cr I phase transforms into a different crystalline phase, which we term Cr II in this paper. The long spacing of Cr II is 4.84 nm, which is almost twice as large as that of Cr I, because the peak of the 001 reflection is located at q = 1.30 nm^{-1}. Hence, the structure of the Cr II phase is assumed to be a double bilayer, as described earlier. An extended bilayer structure is another possibility. It should be noted here that Figure 1a seems to lack a signal corresponding to the phase transition from Cr I to Cr II in the total heat flow for the first heating process. This apparent inconsistency in DSC and X-ray scattering data regarding on Cr

DOI: 10.1021/acs.jpcb.6b03804
J. Phys. Chem. B 2016, 120, 5291−5300

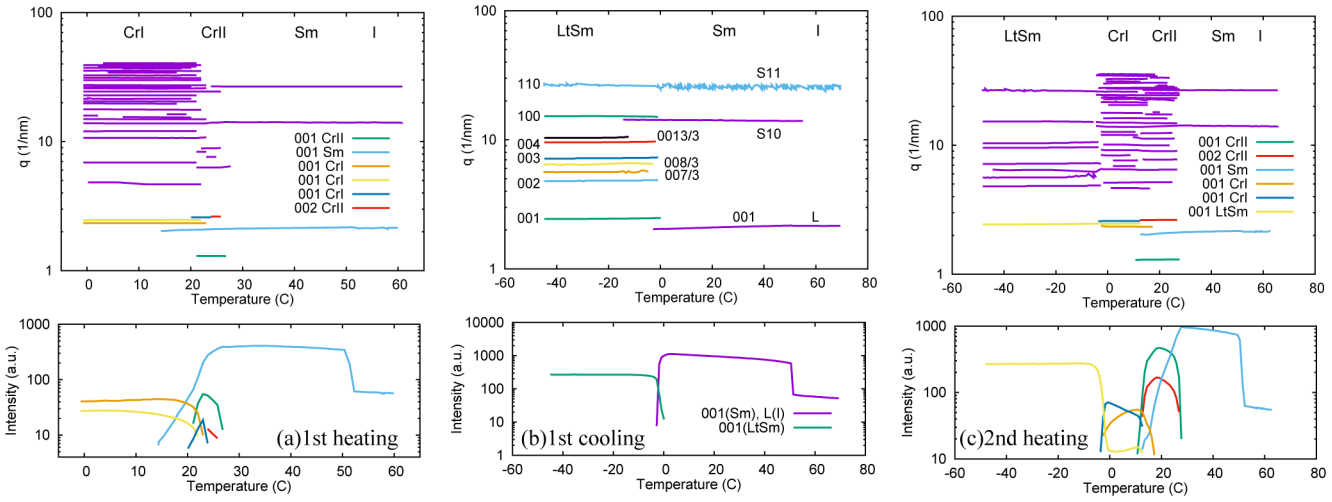

Figure 3. Temperature dependence of the peak positions in the q space (upper) and their observed intensity (lower) for the (a) first heating, (b) first cooling, and (c) second heating processes for $[C_{12}mim]BF_4$. The ramping rate was 10 K/min. Top: peak positions observed for both the SAXS and WAXS measurements. Bottom: scattering intensities observed only for the SAXS regions.

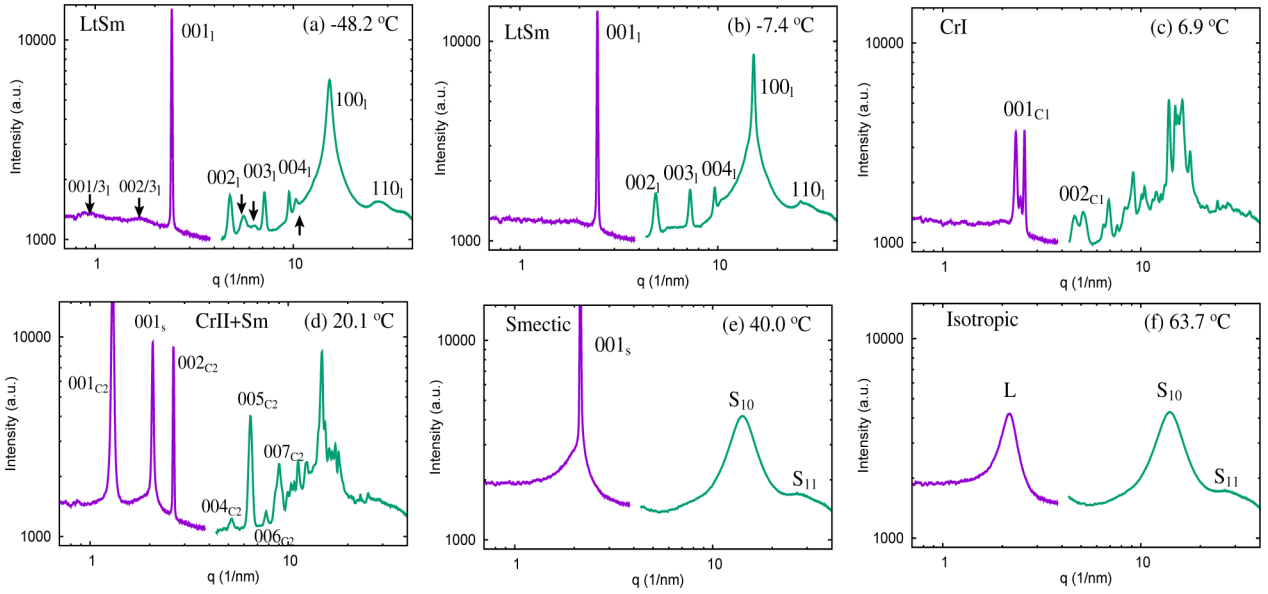

Figure 4. Observed patterns for both the SAXS and WAXS measurements for the second heating processes for $[C_{12}mim]BF_4$ at various temperatures: (a) −48.2, (b) −7.4, (c) 6.9, (d) 20.1, (e) 40.0, and (f) 63.7 °C. Scattering patterns in (a) and (b) are the same as those at −48.2 and −7.4 °C, respectively, for the first cooling process. Scattering patterns in (e) and (f) are the same as those observed at 40.0 and 63.7 °C for the first heating and cooling process, respectively.

II phase for the first heating process may be caused by the thermal history and very slow dynamics characteristic of the sample and the phase changes governed by such slow dynamics cannot be followed by the fast DSC scanning rate such as 10 K/mim.

Above 27 °C, there is only one sharp reflection, which corresponds to the long spacing of the Sm phase (Figures 3a and 4e). The peak position of the long spacing in the q space changes from 2.02 to 2.17 nm^{-1} with increasing temperature, suggesting that the long spacing has a strong temperature dependence. The degree of interdigitation should be strongly dependent on the temperature. The Sm phase has broad peaks at 14.0 nm^{-1} (S10) and 26.7 nm^{-1} (S11) in the WAXS region, corresponding to short-range order of hexagonal side-packing. The ratio of the lattice spacings of S10 and S11 is approximately $\sqrt{3}$.

At the end of the first heating process, the Sm phase changes into the I phase at 51 °C. The I phase has two types of short-range order (Figure 4f). One is shown by a broad peak at 2.1 nm^{-1}, which corresponds to short-range longitudinal order (L). This suggests a roughly preferred orientation, and a layered structure with high roughness even in the liquid state, as suggested previously.[18,19] The other type is shown by two broad peaks, S10 and S11, similar to those for the Sm phase.

First Cooling Process. In this process, the I phase changes to the Sm phase at 51 °C. The Sm phase does not change into the Cr I or the Cr II phase but into another solid-like phase at ca. 0 °C through the supercooled Sm phase. The SAXS and WAXS scattering patterns from the structure of this solid-like phase are similar to those given in Figure 4b. There is a sharp reflection corresponding to a periodic layered structure in the SAXS region. Not only the first-order reflection, 001, but also higher-

DOI: 10.1021/acs.jpcb.6b03804
J. Phys. Chem. B 2016, 120, 5291−5300

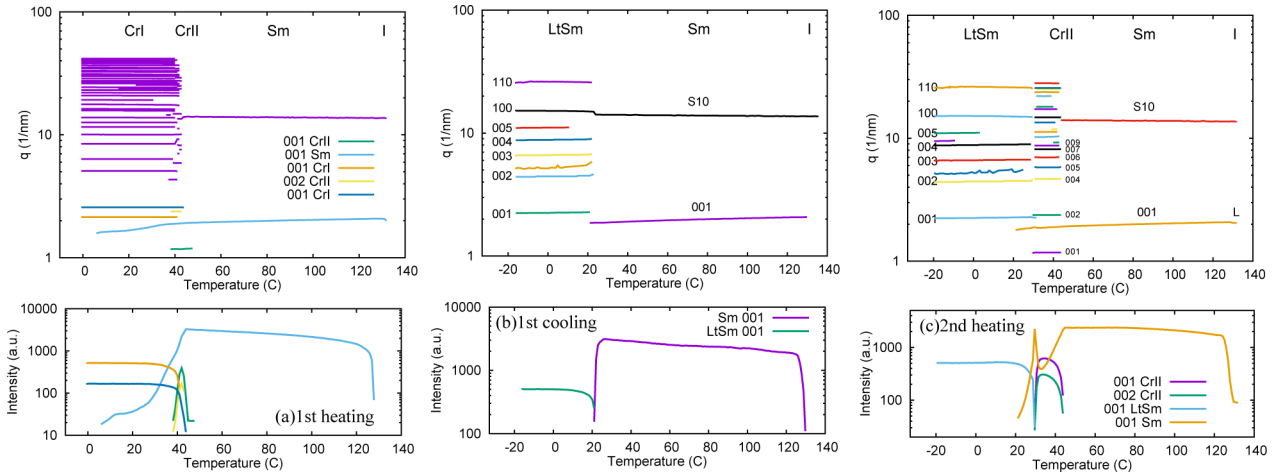

Figure 5. Temperature dependence of the peak positions in the q space (upper) and their observed intensities (lower) for the (a) first heating, (b) first cooling, and (c) second heating processes for $[C_{14}mim]BF_4$. The ramping rate was 10 K/min.

order reflection, such as 002, 003, and 004, can be observed in the WAXS region. This suggests that the order of lamellar stacks is much higher than that of the smectic phase. On the other hand, there are sharp peaks, 100 and 110, on a very broad background for the lateral ordering, indicating paracrystalline order instead of long-range order along the direction perpendicular to the alkyl chains.[20,21] This phase can be observed in the low-temperature region below that of the Sm phase during the cooling process. In this paper, this phase is termed the low-temperature smectic (LtSm) phase. The structure of this phase may be similar to that of the smectic X or smectic T phases.[10,22−25] The degree of structural order of the LtSm phase is higher than that of the Sm phase, but it is lower than that of the crystalline phases.

Upon further cooling in the LtSm phase, the structure changes with decreasing temperature; at ca. −50 °C, weak satellite reflections appear at the locations of $00m/3$, where m is a positive integer. This suggests that weak modulation with a period corresponding to three layers affects the structure of the stacked layers, as shown by the arrows in Figure 4a.

Second Heating Process. In this process, the structure of the LtSm phase changes up to −2 °C in a way similar to that observed for the preceding cooling process. At −2 °C, many sharp Bragg reflections characteristic of the Cr I phase appear, and their intensities increase with increasing temperatures (Figure 4c). After the Cr I phase is transformed into the Cr II phase at 14 °C (Figure 4d), the Cr II phase is further transformed into the Sm phase at 27 °C and finally into the I phase at 52 °C. DSC results in Figure 1c show the existence of the first exothermic, first endothermic, second endothermic, and third endothermic peaks at −1.3, 12.0, 29.6, and 51.6 °C, respectively. The four thermal signals correspond to the phase changes described by LtSm → Cr I → Cr II → Sm → I.

Phase Behavior in $[C_{14}mim]BF_4$. The change with temperature of the peak positions and intensities observed in the X-ray scattering pattern for $[C_{14}mim]BF_4$ are shown in Figure 5. The phase behavior during the first heating and cooling processes is the same as that for $[C_{12}mim]BF_4$, except that the transition temperatures among the five different phases, i.e., the Cr I, Cr II, Sm, I, and LtSm phases, are different from those for $[C_{12}mim]BF_4$ (Figure 5a,b). For example, the transition observed at 123.9 °C is the I-to-Sm phase transition, and that at 25.1 °C is the Sm-to-LtSm phase transition.

For the subsequent second heating process, the change with temperature in the SAXS region is as follows (Figure 5c): The scattering intensity of the SAXS peak of the LtSm phase at 2.3−2.4 nm^{-1} due to the long period 001 begins to decrease with increasing temperature at 20 °C. Meanwhile, the scattering intensity of the peak due to the long period at 1.8−2.1 nm^{-1} of the Sm phase increases with increasing temperature. This corresponds to the phase change or disordering process from the LtSm phase to the Sm phase. As shown in Figure 1c, the total heat flow measured by DSC begins to decrease at around 20 °C and then increases with increasing temperature, leading to an existence of endothermic peak at 28.7 °C. The X-ray result is thus consistent with the DSC measurements.

At 31 °C, two SAXS peaks appear at q = 1.2 and 2.4 nm^{-1}, in addition to the peak at 1.9 nm^{-1}. The two peaks come from the long period of the crystalline phase Cr II. Their intensities associated with Cr II show maxima with increasing temperature, disappearing at 48 °C. At the same time, the intensity of the SAXS peak for the Sm phase initially decreases and then increases. This suggests that a fraction of the Sm phase changes to the Cr II phase only between 31 and 48 °C. The DSC results indicate that the total heat flow decreases again at 35 °C, leading to the first exothermic peak and later increases with increasing temperature, leading to the second endothermic peak at 44.4 °C.

A third endothermic peak associated with the Sm-to-I phase transition also exists at 125.4 °C. Consequently, the intensity of the 001 reflection of the Sm phase decreases very rapidly at around 125 °C.

Phase Behavior of $[C_{16}mim]BF_4$ and $[C_{18}mim]BF_4$. As shown in Figure 1, the phase behavior of $[C_{16}mim]BF_4$ and $[C_{18}mim]BF_4$ is simpler than that of $[C_{12}mim]BF_4$ and $[C_{14}mim]BF_4$. During the first heating process, the samples change from the Cr I(or Cr II) phase to the I phase via the Sm phase. In the first cooling process, the I phase is transformed to the Sm phase and then to the LtSm phase via a supercooled Sm state. The structure of the LtSm phase is the same as that shown in Figure 4b, except for the lattice spacing. During the second heating process, the LtSm phase transforms to the Sm phase without showing any crystalline phase, in contrast to the observation for $[C_{12}mim]BF_4$ and $[C_{14}mim]BF_4$.

OM. The DSC and X-ray results show that crystalline phases appear between the LtSm phase and Sm phase during the

DOI: 10.1021/acs.jpcb.6b03804
J. Phys. Chem. B 2016, 120, 5291−5300

second heating process for $[C_{12}mim]BF_4$ and $[C_{14}mim]BF_4$. OM measurements were thus performed to verify whether the crystalline phases appear within the LtSm phase. Figure 6

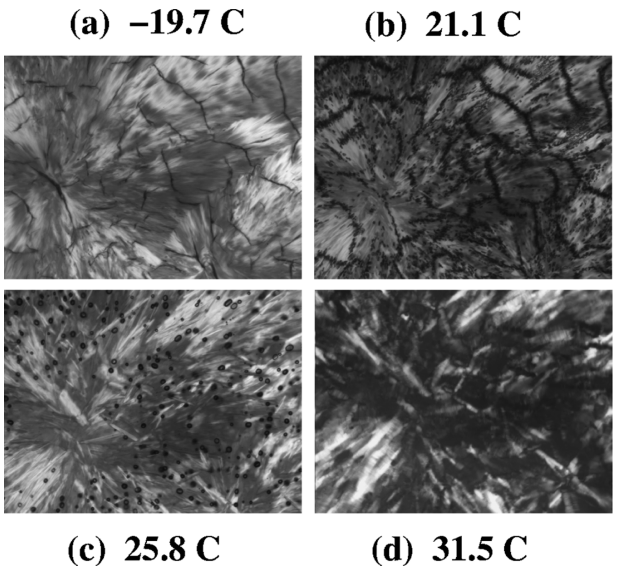

Figure 6. Optical microscopy images for $[C_{12}mim]BF_4$ obtained under the crossed Nicol condition at the temperatures of (a) −19.7, (b) 21.1, (c) 25.8, and (d) 31.5 °C. The horizontal length of each OM image corresponds to 330 μm.

shows an example of the OM images of $[C_{12}mim]BF_4$ obtained under the crossed Nicol condition at −19.7 to 31.5 °C during the second heating process at 5 K/min ramping rate, which was after the first cooling process at the same rate. At −19.7 °C, the sample is in the LtSm phase. At 21.1 °C, it is in the Cr II phase, and small droplets appear along black lines. The number and size of the droplets increase with increasing temperature. At 25.8 °C, the small droplets coalescence to larger droplets. At 31.5 °C, the droplets disappear in the Sm phase. The change in the number and size of the droplets corresponds to the temperature change in the intensity of the SAXS peaks due to the long period of Cr II. Hence, the droplets may be regarded as crystalline regions of the Cr II phase. Two-dimensional SAXS patterns clearly show the existence of continuous Debye−Scherrer rings. Therefore, the droplets in Figure 6 may not be single crystals but instead polycrystals of the Cr II phase. Nearly identical OM images for $[C_{14}mim]BF_4$ were obtained for the second heating process. These images clearly show that a fraction of the crystalline phases appears within the LtSm phases.

Phase Diagram of $[C_n mim]BF_4$. From the DSC, X-ray scattering, and OM measurements, $[C_n mim]BF_4$ (n = 12, 14, 16, 18) was found to exhibit characteristic phase behavior depending on n. Figure 7 shows the n dependence of the transition temperatures for the first heating and cooling processes and subsequent second heating process. The two transition temperatures for the first heating process increase with increasing n, and the rate of increase in the Sm-to-I transition temperature with respect to n is greater than that in the Cr-to-Sm transition temperature (○ and □ in Figure 7a). Hence, the temperature range of the Sm phase becomes larger with increasing n. The Sm-to-LtSm transition temperature (▽) during the first cooling process is lower than the Cr-to-Sm transition temperature (□) during the first heating process at a

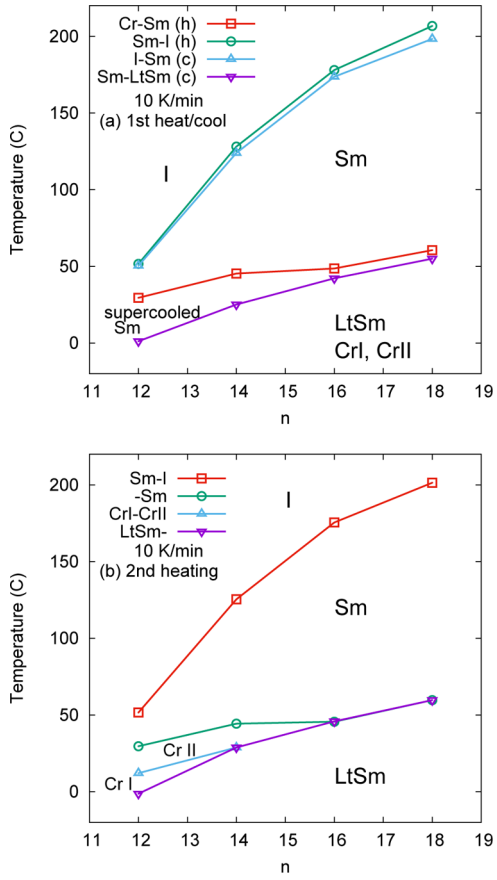

Figure 7. Dependence of transition temperature on the number of alkyl carbon atoms n of $[C_n mim]BF_4$, as obtained by DSC during (a) the first heating and cooling processes and (b) the second heating process at 10 K/min. In (a), symbols □ and ○ respectively represent the Cr-to-Sm and the Sm-to-I transition temperatures during the first heating process. The symbols △ and ▽ respectively represent the I-to-Sm and the Sm-to-LtSm transition temperatures during the first cooling process. In (b), symbols ▽, △, ○, and □ respectively represent the temperatures for LtSm-to-Cr I, Cr II, or Sm transition; Cr I-to-Cr II transition; Cr II-to-Sm transition; and Sm-to-I transition during the second heating process.

given n. This result suggests the existence of supercooling of the Sm phase in the first cooling process. Furthermore, the degree of supercooling of the Sm phase increases with decreasing n, which may be related to the characteristic phase behavior during the second heating process with n = 12 and 14.

During the second heating process, the LtSm-to-Cr I, Cr II, or Sm transition (▽) occurs around the Sm-to-LtSm transition temperature observed during the first cooling process (Figure 7b). Subsequently, the Cr I-to-Cr II and Cr II-to-Sm transition of $[C_{12}mim]BF_4$ as well as the Cr II-to-Sm transition of $[C_{14}mim]BF_4$ occur. Finally, the Sm-to-I transition for both cases takes place. It should be noted that the Cr II- and LtSm-to-Sm transition temperatures are nearly equal to the Cr II-to-Sm transition temperature observed during the first heating process. These results suggest that the temperature range for the existence of the Cr I and Cr II phases is restricted to the supercooled region of the Sm phase observed during the first cooling process.

From the phase diagram in Figure 7, the plausible free energy of each phase can be estimated. Figure 8 shows schematic diagrams of the temperature dependence of the Gibbs free

DOI: 10.1021/acs.jpcb.6b03804
J. Phys. Chem. B 2016, 120, 5291−5300

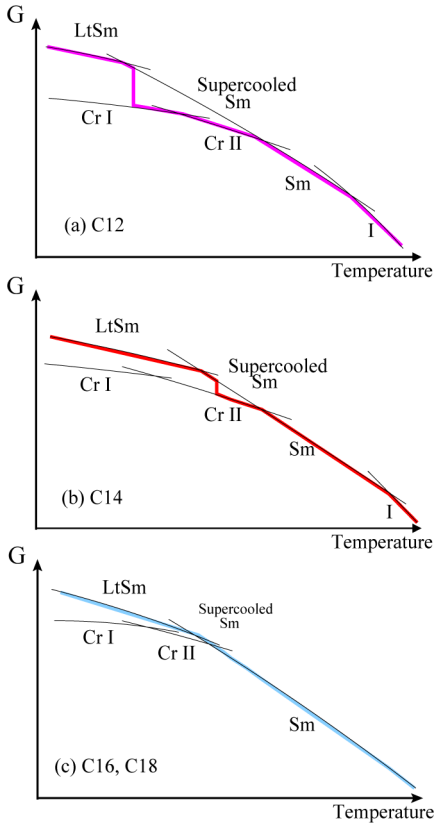

Figure 8. Schematic diagrams of Gibbs free energy vs the temperature for various phases for $[C_n\text{mim}]BF_4$ observed during the second heating process: (a) n = 12, (b) n = 14, and (c) n = 16 and 18. Purple, red, and blue curves correspond to the paths observed during the second heating process for n = 12, 14, and 16, 18, respectively.

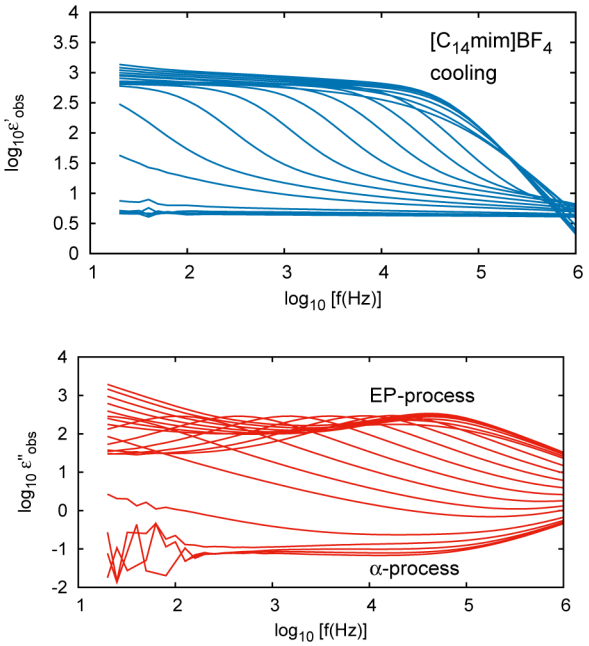

Figure 9. Dependence of the observed complex dielectric permittivity on the logarithm of the frequency of the applied electric field at various temperatures during the cooling process for $[C_{14}\text{mim}]BF_4$. Selected temperatures for curves from right to left: 120.7, 105.9, 91.0, 76.3, 61.5, 46.8, 32.2, 22.7, 17.8, 12.9, 8.1, 3.3, −1.5, −6.2, −11.0, −25.5, −40.0, −53.8, −63.6, and −69.9 °C.

energy for the various observed phases of $[C_n\text{mim}]BF_4$ (n = 12, 14, and 16, 18). Each curve represents the temperature dependence of the Gibbs free energy of the corresponding phase. For the first cooling process, the Sm phase of $[C_n\text{mim}]BF_4$ shows supercooling, with the degree of supercooling increasing with decreasing n. Hence, the Gibbs free energy of the LtSm phase is higher than that of Cr I and Cr II, and the LtSm phase is a metastable phase. In the second heating process, the Gibbs free energy of this system changes along the colored curves in a different manner depending on the number n. The LtSm phase can be obtained only from the supercooled Sm phase. Because the structure of the LtSm phase is more ordered than that of the Sm phase but less ordered than that of the Cr I or Cr II phase, the LtSm phase may be reasonably assumed to be obtained from the incomplete freezing of the supercooled smectic phase.

Motion of Charge Carriers and Phase Behavior. In the preceding sections, we have established that $[C_n\text{mim}]BF_4$ exhibits characteristic phase behavior related to the existence of the LtSm phase after supercooling of the Sm phase on cooling. Here, the dynamics related to this phase behavior have been investigated by DRS. In this system, molecular motion of charge carriers, which may be ions or other charged particles, have strong contributions to dielectric relaxation phenomena. In this case, molecular motion of $[C_n\text{mim}]BF_4$ also contributes. Figure 9 shows the dependence of the observed complex dielectric permittivity ε^*_{obs} of $[C_{14}\text{mim}]BF_4$ on the frequency of the applied electric field during the cooling process at 1 K/min rate from 120.7 to −69.9 °C. Here, ε^*_{obs} is defined as $\varepsilon^*_{obs} = C^*_{mes}/C_0$, where $\varepsilon^*_{obs} = \varepsilon'_{obs} - i\varepsilon''_{obs}$. At high temperatures, there are dielectric signals with the strength of $\varepsilon'_{obs} \sim 10^3$. The large values of ε'_{obs} and ε''_{obs} can be attributed to charge-carrier-related phenomena such as Maxwell−Wagner−Sillar (MWS) interfacial polarization process and electrode polarization (EP) process.[26−33] Because of the existence of loss peaks of ε''_{obs} for all of the phases, including the I phase, large loss peaks may be reasonably attributed to the EP-process. The physical origin of the EP-process is the blocking of the charge carriers on the electrodes; the motion of charge carriers is essential to this process. At low temperatures, there is another loss signal, which is due to the α-process of $[C_n\text{mim}]BF_4$.[34] In this system, there is a secondary relaxation proces at an even lower temperature,[35] but this process is likely to occur beyond the present frequency window. On the high-frequency side, ε''_{obs} increases with increasing frequency. This increase, which is independent of the temperature, can be attributed to the electrical resistance of the electrode.

In our analysis, we assumed that the complex dielectric permittivity $\varepsilon^*(\omega)$ can be described by the sum of the two contributions, i.e., the EP- and α-processes, after removal of the contribution by the electrical resistance of the electrodes:

$$\varepsilon^*(\omega) = \sum_{i=\text{ep},\alpha} \frac{\Delta\varepsilon_i}{(1 + (i\omega\tau_i)^{\alpha_i})^{\beta_i}} + \varepsilon_\infty \quad (2)$$

where the dielectric spectra of the EP- and α-processes are described by the Havriliak−Negami equation.[36] α_i and β_i are the shape parameters of the i-th mode; τ_i and $\Delta\varepsilon_i$ are the relaxation time and dielectric relaxation strength, respectively, of the i-th mode; and ε_∞ is the dielectric permittivity at very high frequency. The observed dielectric permittivity ε^*_{obs} can well be reproduced using eqs 1 and 2, and the relaxation times

DOI: 10.1021/acs.jpcb.6b03804
J. Phys. Chem. B 2016, 120, 5291−5300

and dielectric relaxation strengths of the EP- and α-processes (τ_{ep}, τ_α and $\Delta\varepsilon_{ep}$, $\Delta\varepsilon_\alpha$, respectively) are obtained as functions of temperature.

Figure 10 shows the dependence of the relaxation times of the EP-process (τ_{ep}) and α-process (τ_α) on the inverse of the temperature for both the first cooling and subsequent second heating processes for $[C_{14}mim]BF_4$ and $[C_{16}mim]BF_4$.

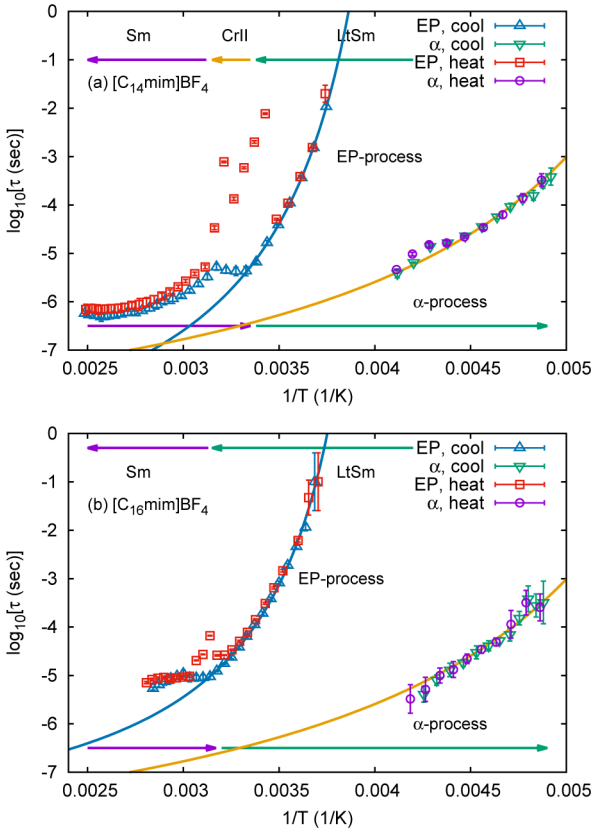

Figure 10. Dependence of the relaxation times of the EP- and α-processes on the inverse of temperature during the cooling and the subsequent heating process for (a) $[C_{14}mim]BF_4$ and (b) $[C_{16}mim]BF_4$. The symbols △, ▽, □, and ○ correspond to the EP- and α-processes for the cooling process and the EP- and α-processes for the heating process, respectively. The curves are given by fitting the observed data to eq 3.

For $[C_{14}mim]BF_4$, Figure 10a shows that during the first cooling process from the I phase, τ_{ep} increases gradually with decreasing temperature in the Sm phase. Then, it begins to increase rapidly at 28 °C and continues to increase with decreasing temperature in the LtSm phase. As the temperature further decreases after the disappearance of the signal from the EP-process, the α-process occurs at low temperatures, and the relaxation time of the α-process increases with decreasing temperature. The temperature dependences of both τ_{ep} and τ_α are found to be described by the Vogel−Fulcher−Tammann (VFT) law[37−40]

$$\tau_i(T) = \tau_{0,i} \exp\left(\frac{U_i}{T - T_{0,i}}\right) \quad (i = \alpha, \text{ ep}) \tag{3}$$

which has a much stronger temperature dependence than that of the Arrhenius law. Here, $\tau_{0,i}$ and U_i are positive constants, and $V_{0,i}$ is the Vogel temperature at which τ_i diverges. In the present study, the frequency window of the DRS measurements had to be restricted in order to perform the measurements under a ramping rate of 1 K/min. Nevertheless, we carried out fitting to reproduce the temperature dependence of τ_{ep} and τ_α in the LtSm phase using eq 3. We obtained good reproduction of this behavior, as shown by the curves in Figure 10. The best fitting parameters of the VFT law are given in Table 2.

Table 2. Parameters of the VFT Law for the EP- and α-Processes in the LtSm Phase of $[C_{14}mim]BF_4$ and $[C_{16}mim]BF_4$

	EP-process		α-process[a]
	n = 14	n = 16	n = 14, 16
log $\tau_{0,i}$ (s)	−9.2 ± 0.3	−7.8 ± 0.4	−8.2 ± 0.8
U_i (K)	623 ± 76	510 ± 80	605 ± 271
$T_{0,i}$ (K)	229 ± 3	238 ± 4	149 ± 15

[a]The parameters for the α-process were evaluated by using data for both $[C_{14}mim]BF_4$ and $[C_{16}mim]BF_4$.

From the fitting parameters, the glass transition temperature, T_g, of $[C_nmim]BF_4$ can be evaluated as the temperature at which the relaxation time of the α-process becomes a macroscopic time scale, τ_{macro}. If we select $\tau_{macro} \sim 10^2$ s, we obtain T_g = 175 ± 6 K. This T_g value agrees well with that determined in the literature,[34] although the frequency range used in this study is limited. Within the present experimental accuracy, determining any dependence of T_g on n is difficult. Furthermore, the Vogel temperatures of the EP-process are 229 and 238 K for n values of 14 and 16, respectively, and that of the α-process is 149 K. These results suggest that the molecular motion in the α-process is frozen after the cessation of charge-carrier motion during the cooling process. In other words, the motion of charge carriers is decoupled from the α-process.[33]

During the heating process, the relaxation time τ_{ep} decreases with increasing temperature up to 17 °C in the same way as τ_{ep} during the preceding cooling process. τ_{ep} then begins to increase very rapidly with increasing temperature at 17 °C and then decreases again with increasing temperature. Above 46 °C, τ_{ep} overlaps with that observed for the preceding cooling process. Because the temperature range from 17 and 46 °C corresponds to that of the Cr II phase, τ_{ep} of the Cr II phase is larger than that of the LtSm phase and the supercooled Sm phase at a given temperature. This suggests that the motion of charge carriers in the Cr II phase is slower than that in the LtSm phase.

From the observed temperature dependence of τ_{ep} and τ_α in Figure 10a, the following scenario may be proposed for the relationship between the molecular dynamics and the phase change for $[C_{14}mim]BF_4$. During the first cooling process, the motion of charge carriers becomes slower with decreasing temperature. As the reduction of the motion of charge carriers reaches a critical value, transition from the Sm phase to the LtSm phase occurs through the supercooled Sm phase. In the LtSm phase, the charge carriers are still mobile because of the α-process. As the temperature decreases further, the motion of charge carriers freezes above T_g, and then the α-process freezes so that a glassy state of the LtSm phase can be obtained. During the subsequent heating process, the α-process activates above T_g, thus facilitating the activation of motion of charge carriers. When the mobility due to charge carrier motion increases and reaches a certain value, the Cr II phase crystallizes within the supercooled Sm phase. Finally, Cr II-to-Sm phase transition

DOI: 10.1021/acs.jpcb.6b03804
J. Phys. Chem. B 2016, 120, 5291−5300

occurs. The change in motion of charge carriers with temperature is highly correlated with that of the phase behavior.

Figure 10b shows the temperature dependence of τ_{ep} and τ_{α} during the first cooling and the subsequent heating processes for $[C_{16}mim]BF_4$. In this case, the temperature dependence of τ_{ep} during the cooling process agrees very well with that of the subsequent heating process, except for temperature range around the LtSm-to-Sm phase transition during the heating process. This suggests that the proposed scenario for the relationship between the molecular dynamics and the phase change is also applicable to $[C_{16}mim]BF_4$. A small increase in τ_{ep} around 40 °C may correspond to a change from the LtSm phase to the Cr II phase. However, the Sm phase appears with increasing temperature before the phase change is complete because the temperature range of the supercooled Sm phase in $[C_{16}mim]BF_4$ is much smaller than that of the supercooled Sm phase in $[C_{14}mim]BF_4$.

CONCLUDING REMARKS

In this study, the phase transition behavior and molecular motion of imidazolium-based ILCs, 1-methyl-3-alkyl-imidazolium tetrafluoroborate $[C_nmim]BF_4$ (n = 12, 14, 16, 18) were investigated by DSC, X-ray scattering, OM, and DRS. The obtained results are summarized as follows:

1. During the cooling process from the I phase through the Sm phase, the metastable LtSm phase was obtained via the supercooled Sm phase. The structural order of the LtSm phase is lower than that of the crystalline phases but higher than that of the Sm phase.

2. During the subsequent heating process, the LtSm phase changes into a crystalline phase, Cr II (for n = 14), or to the other crystalline phases Cr I and then Cr II (for n = 12) at the temperature at which the supercooled Sm phase has changed into the LtSm phase during the preceding cooling process. The Sm phase then appears.

3. The relaxation time of the charge carrier motion in $[C_{14}mim]BF_4$ increases up to a certain value with decreasing temperature in the supercooled Sm phase during the cooling process and then increases more rapidly with decreasing temperature during the phase change into the LtSm phase. With further decrease in temperature, the motion of the charge carriers first freezes, and then the α-process freezes so that a glassy state can be obtained. During the subsequent heating process, the motion of charge carriers is activated only after the α-process has been activated. The relaxation time of the charge carrier motion reaches a certain value, and crystallization then occurs in the LtSm phase. Finally, the ILC is transformed into the Sm phase and then into the I phase with increasing temperature.

A few remarks regarding the MWS process can be made. Although the assignment of the large dielectric loss to the EP-process is mostly valid in the present ILCs, the contribution from the MWS-process for the Cr I or Cr II phase may not be negligible during the second heating process for $[C_{14}mim]BF_4$, in which droplets of the crystalline phase exist in the LtSm phase. In such a domain structure, not only the EP-process but also the MWS-process may be activated.[41]

On the other hand, the microscopic origin of the EP-process is related to the translational diffusion motion of charge carriers. As such, the dependence of $\Delta\varepsilon_{ep}$ and τ_{ep} on the distance d between the two electrodes can be converted into the diffusion constant of the charge carrier on the basis of a theoretical model.[42] The model suggests that both $\Delta\varepsilon_{ep}$ and τ_{ep} should be linear functions of d. Hence, DRS measurements for various d values will be essential to further analysis of the molecular motion of the charge carriers. A linear relationship between $\Delta\varepsilon_{ep}$ (τ_{ep}) and d would be strong evidence for the assignment of the present loss signal to the EP-process.

In the present study, we used an ITO glass substrate covered with polyimide after rubbing treatment for the preferred parallel orientation, as a sample cell for DRS measurements. For comparison, we attempted to perform dielectric measurements using an ITO glass substrate covered with polyimide without rubbing treatment. Preliminary results indicate that the dielectric strength and relaxation time of the EP-process depend on the rubbing treatment. In other words, the motion of charge carriers may depend on the orientation of $[C_nmim]BF_4$. Detailed measurements will be performed in order to elucidate the dependence of the molecular dynamics and the phase behavior on the orientation.

AUTHOR INFORMATION

Corresponding Author

*E-mail fukao.koji@gmail.com; Ph +81 (0)77 5612720; Fax +81 (0)77 5612720 (K.F.).

Present Addresses

K.S.: Faculty of Life and Medical Sciences, Doshisha University, Kyotanabe 610-0321, Japan.

K.N.: DIC Corporation, Central Research Laboratories, 631 Sakado, Sakura 285-8668, Japan.

Notes

The authors declare no competing financial interest.

ACKNOWLEDGMENTS

This work was partially supported by a Grant-in-Aid for Scientific Research (B) (No. 25287108) and Exploratory Research (No. 25610127) from the Japan Society for the Promotion of Science. The synchrotron radiation experiments were performed at the BL40B2 of SPring-8 with the approval of the Japan Synchrotron Radiation Research Institute (JASRI) (Proposals 2013A1173, 2014A1230 and 2015B1192).

REFERENCES

(1) Earle, M. J.; Esperança, J. M.; Gilea, M. A.; Lopes, J. N. C.; Rebelo, L. P.; Magee, J. W.; Seddon, K. R.; Widegren, J. A. The Distillation and Volatility of Ionic Liquids. *Nature* **2006**, *439*, 831−834.

(2) MacFarlane, D. R.; Pringle, J. M.; Johansson, K. M.; Forsyth, S. A.; Forsyth, M. Lewis Base Ionic Liquids. *Chem. Commun.* **2006**, 1905−1917.

(3) Kagimoto, J.; Taguchi, S.; Fukumoto, K.; Ohno, H. Hydrophobic and Low-density Amino Acid Ionic Liquids. *J. Mol. Liq.* **2010**, *153*, 133−138.

(4) Bonhôte, P.; Dias, A.-P.; Papageorgiou, N.; Kalyanasundaram, K.; Grätzel, M. Hydrophobic, Highly Conductive Ambient-Temperature Molten Salts. *Inorg. Chem.* **1996**, *35*, 1168−1178.

(5) Marsh, K.; Boxall, J.; Lichtenthaler, R. Room Temperature Ionic Liquids and Their Mixtures - a Review. *Fluid Phase Equilib.* **2004**, *219*, 93−98.

(6) Ghandi, K. A Review of Ionic Liquids, Their Limits and Applications. *Green Sustainable Chem.* **2014**, *4*, 44−53.

(7) Gordon, C. M.; Holbrey, J. D.; Kennedy, A. R.; Seddon, K. R. Ionic Liquid Crystals: Hexafluorophosphate Salts. *J. Mater. Chem.* **1998**, *8*, 2627−2636.

(8) Holbrey, J. D.; Seddon, K. R. The Phase Behaviour of 1-Alkyl-3-methylimidazolium Tetrafluoroborates; Ionic Liquids and Ionic Liquid Crystals. *J. Chem. Soc., Dalton Trans.* **1999**, 2133−2140.

DOI: 10.1021/acs.jpcb.6b03804
J. Phys. Chem. B 2016, 120, 5291−5300

(9) Hardacre, C.; Holbrey, J. D.; McCormac, P. B.; McMath, S. E. J.; Nieuwenhuyzen, M.; Seddon, K. R. Crystal and Liquid Crystalline Polymorphism in 1-Alkyl-3-methylimidazolium Tetrachloropalladate-(ii) Salts. *J. Mater. Chem.* **2001**, *11*, 346−350.
(10) Yoshio, M.; Mukai, T.; Kanie, K.; Yoshizawa, M.; Ohno, H.; Kato, T. Liquid-Crystalline Assemblies Containing Ionic Liquids: An Approach to Anisotropic Ionic Materials. *Chem. Lett.* **2002**, *31*, 320−321.
(11) Bradley, A. E.; Hardacre, C.; Holbrey, J. D.; Johnston, S.; McMath, S. E. J.; Nieuwenhuyzen, M. Small-Angle X-ray Scattering Studies of Liquid Crystalline 1-Alkyl-3-methylimidazolium Salts. *Chem. Mater.* **2002**, *14*, 629−635.
(12) De Roche, J.; Gordon, C. M.; Imrie, C. T.; Ingram, M. D.; Kennedy, A. R.; Lo Celso, F.; Triolo, A. Application of Complementary Experimental Techniques to Characterization of the Phase Behavior of $[C_{16}mim][PF_6]$ and $[C_{14}mim][PF_6]$. *Chem. Mater.* **2003**, *15*, 3089−3097.
(13) Downard, A.; Earle, M. J.; Hardacre, C.; McMath, S. E. J.; Nieuwenhuyzen, M.; Teat, S. J. Structural Studies of Crystalline 1-Alkyl-3-methylimidazolium Chloride Salts. *Chem. Mater.* **2004**, *16*, 43−48.
(14) Li, L.; Groenewold, J.; Picken, S. J. Transient Phase-Induced Nucleation in Ionic Liquid Crystals and Size-Frustrated Thickening. *Chem. Mater.* **2005**, *17*, 250−257.
(15) Xu, F.; Matsumoto, K.; Hagiwara, R. Effects of Alkyl Chain Length on Properties of 1-Alkyl-3-methylimidazolium Fluorohydrogenate Ionic Liquid Crystals. *Chem. - Eur. J.* **2010**, *16*, 12970−12976.
(16) Wang, M.; Pan, X.; Xiao, S.; Zhang, C.; Li, W.; Dai, S. Regulating Mesogenic Properties of Ionic Liquid Crystals by Preparing Binary or Multi-component Systems. *J. Mater. Chem.* **2012**, *22*, 2299−2305.
(17) Xu, F.; Matsumoto, K.; Hagiwara, R. Effects of Alkyl Chain Length and Anion Size on Thermal and Structural Properties for 1-Alkyl-3-methylimidazolium Hexafluorocomplex Salts (CxMImAF6, x = 14, 16 and 18; A = P, As, Sb, Nb and Ta). *Dalton Trans.* **2012**, *41*, 3494−3502.
(18) Kofu, M.; Nagao, M.; Ueki, T.; Kitazawa, Y.; Nakamura, Y.; Sawamura, S.; Watanabe, M.; Yamamuro, O. Heterogeneous Slow Dynamics of Imidazolium-Based Ionic Liquids Studied by Neutron Spin Echo. *J. Phys. Chem. B* **2013**, *117*, 2773−2781.
(19) Nemoto, F.; Kofu, M.; Yamamuro, O. Thermal and Structural Studies of Imidazolium-Based Ionic Liquids with and without Liquid-Crystalline Phases: The Origin of Nanostructure. *J. Phys. Chem. B* **2015**, *119*, 5028−5034.
(20) Fukao, K. X-ray Scattering and Disordered Structure of n-Tetracosane in Urea Adducts. I. A Model for the X-ray Scattering Pattern. *J. Chem. Phys.* **1994**, *101*, 7882−7892.
(21) Fukao, K. X-ray Scattering and Disordered Structure of n-Tetracosane in Urea Adducts. II. Averaged Disorder, Spatial Correlation, and Phase Transition. *J. Chem. Phys.* **1994**, *101*, 7893−7903.
(22) Arkas, M.; Tsiourvas, D.; Paleos, C. M.; Skoulios, A. Smectic Mesophases from Dihydroxy Derivatives of Quaternary Alkylammonium Salts. *Chem. - Eur. J.* **1999**, *5*, 3202−3207.
(23) Chakin, P. M.; Lubensky, T. C. *Principles of Condensed Matter Physics*; Cambrigde University Press: Cambridge, UK, 2000.
(24) Goossens, K.; Lava, K.; Nockemann, P.; Van Hecke, K.; Van Meervelt, L.; Driesen, K.; Görller-Walrand, C.; Binnemans, K.; Cardinaels, T. Pyrrolidinium Ionic Liquid Crystals. *Chem. - Eur. J.* **2009**, *15*, 656−674.
(25) Tripathi, C. S. P.; Leys, J.; Losada-Pérez, P.; Lava, K.; Binnemans, K.; Glorieux, C.; Thoen, J. Adiabatic Scanning Calorimetry Study of Ionic Liquid Crystals with Highly Ordered Crystal Smectic Phases. *Liq. Cryst.* **2013**, *40*, 329−338.
(26) Schönhals, A.; Kremer, F. In *Broadband Dielectric Spectroscopy*; Kremer, F., Schönhals, A., Eds.; Springer: Berlin, 2003; pp 59−98.
(27) Serghei, A.; Tress, M.; Sangoro, J. R.; Kremer, F. Electrode Polarization and Charge Transport at Solid Interfaces. *Phys. Rev. B: Condens. Matter Mater. Phys.* **2009**, *80*, 184301.
(28) Nakamura, K.; Saiwaki, T.; Fukao, K. Dielectric Relaxation Behavior of Polymerized Ionic Liquid. *Macromolecules* **2010**, *43*, 6092−6098.
(29) Diaham, S.; Locatelli, M.-L. Concentration and Mobility of Charge Carriers in Thin Polymers at High Temperature Determined by Electrode Polarization Modeling. *J. Appl. Phys.* **2012**, *112*, 013710.
(30) Wang, Y.; Sun, C.-N.; Fan, F.; Sangoro, J. R.; Berman, M. B.; Greenbaum, S. G.; Zawodzinski, T. A.; Sokolov, A. P. Examination of Methods to Determine Free-ion Diffusivity and Number Density from Analysis of Electrode Polarization. *Phys. Rev. E* **2013**, *87*, 042308.
(31) Wang, Y.; Fan, F.; Agapov, A. L.; Saito, T.; Yang, J.; Yu, X.; Hong, K.; Mays, J.; Sokolov, A. P. Examination of the Fundamental Relation between Ionic Transport and Segmental Relaxation in Polymer Electrolytes. *Polymer* **2014**, *55*, 4067−4076.
(32) Sangoro, J. R. Charge Transport and Dipolar Relaxations in an Alkali Metal Oligoether Carboxylate Ionic Liquid. *Colloid Polym. Sci.* **2014**, *292*, 1933−1938.
(33) Taniguchi, N.; Fukao, K.; Sotta, P.; Long, D. R. Dielectric Relaxation of Thin Films of Polyamide Random Copolymers. *Phys. Rev. E* **2015**, *91*, 052605.
(34) Kwon, H.-J.; Seo, J.-A.; Iwahashi, T.; Ouchi, Y.; Kim, D.; Kim, H. K.; Hwang, Y.-H. Study of Alkyl Chain Length Dependent Characteristics of Imidazolium Based Ionic Liquids $[C_nMIM]$+[TFSA]- by Brillouin and Dielectric Loss Spectroscopy. *Curr. Appl. Phys.* **2013**, *13*, 271−279.
(35) Rivera, A.; Rössler, E. A. Evidence of Secondary Relaxations in the Dielectric Spectra of Ionic Liquids. *Phys. Rev. B: Condens. Matter Mater. Phys.* **2006**, *73*, 212201.
(36) Havriliak, S.; Negami, S. A Complex Plane Representation of Dielectric and Mechanical Relaxation Processes in Some Polymers. *Polymer* **1967**, *8*, 161−210.
(37) Vogel, H. Das Temperatur-Abhängigkeitsgesetz der Viskosität von Flüssigkeiten. *Phys. Z.* **1921**, *22*, 645−646.
(38) Fulcher, G. S. Analysis of Recent Measurements of the Viscosity of Glasses. *J. Am. Ceram. Soc.* **1925**, *8*, 339−355.
(39) Fulcher, G. S. Analysis of Recent Measurements of the Viscosity of Glasses.II1. *J. Am. Ceram. Soc.* **1925**, *8*, 789−794.
(40) Tammann, G.; Hesse, W. Die Abhängigkeit der Viscosität von der Temperatur bie unterkühlten Flüssigkeiten. *Z. Anorg. Allg. Chem.* **1926**, *156*, 245−257.
(41) Rai, P. K.; Denn, M. M.; Khusid, B. Dielectric Spectroscopy of Liquid Crystalline Dispersions. *Langmuir* **2006**, *22*, 2528−2533.
(42) Coelho, R. Sur la relaxation d'une charge d'espace. *Rev. Phys. Appl.* **1983**, *18*, 137−146.

DOI: 10.1021/acs.jpcb.6b03804
J. Phys. Chem. B 2016, 120, 5291−5300